

Airborne lidar for fisheries applications

James H. Churnside

James J. Wilson

National Oceanic and Atmospheric
Administration (NOAA)
Environmental Technology Laboratory
325 Broadway
Boulder, Colorado 80303
E-mail: jchurnside@etl.noaa.gov

Viatcheslav V. Tatarskii

NOAA

University of Colorado Cooperative Institute
for Research in the Environmental
Sciences
325 Broadway
Boulder, Colorado 80303

Abstract. An airborne lidar using commercial, off-the-shelf components was developed by the National Oceanic and Atmospheric Administration for fisheries' surveys. We make several test flights of the system and develop several signal processing techniques to discriminate between the returns from fish and from small particles in the water. We use these techniques to produce several products of use to fisheries' biologists. Examples are presented of gray-scale images similar to those produced by acoustic echo sounders, of maps of spatial distributions of fish, and of vertical profiles of fish biomass. © 2001 Society of Photo-Optical Instrumentation Engineers. [DOI: 10.1117/1.1348000]

Subject terms: lidar; ocean optics; fish; polarization.

Paper 200045 received Feb. 8, 2000; revised manuscript received Sep. 27, 2000; accepted for publication Sep. 27, 2000.

1 Introduction

The challenge of the fisheries' manager is to set appropriate catch limits so that stocks are not depleted without placing unwarranted financial hardship on fishers and fishing communities. This requires some predictive capability concerning the future state of a particular stock at a particular level of fishing despite large natural fluctuations in populations. Failure to do this can result in the collapse of a fishery.

Stock assessment relies on data from several sources, including information from the fishery about landings and the effort required to achieve those landings and from independent surveys. A research vessel costing \$12,000 per day to perform a fisheries' survey at a speed of 5 kn will cost about \$200/km of survey. A small aircraft costing \$750 per hour and traveling at 150 kn will cost about \$5/km. While the specific details of cost and speed will vary with different ships and different aircraft, these nominal values show a strong incentive for trying to enhance traditional surface-based surveys with airborne components. Visual observations have been used for this purpose, but the results are very limited in depth penetration and depend on viewing conditions. We consider lidar as a technique to improve the depth penetration of airborne fisheries' surveys.

It was observed some time ago that fish could be detected using airborne lidar.¹ Computer models have also suggested that such a system should be able to provide useful information.^{2,3} To test the performance of a lidar system under known conditions, we operated one for three weeks on a ship in the Southern California Bight.⁴ Lidar targets were verified by acoustics and by direct sampling. We demonstrated a procedure to obtain calibrated profiles of fish biomass density.

The calibration procedure requires the reflectivity of fish. Squire and Krumboltz¹ assumed a reflectivity of 50% to estimate the area of fish intercepted by their lidar. Krekova et al.³ follow Murphree et al.² in assuming a reflectivity of 50% for modeling purposes. Fredriksson et al.⁵

measured the lidar return for dead fish, but their system was not calibrated. Benigno and Kemmerer⁶ measured the reflectivity of menhaden in the water at less than 1% across the blue-green portion of the spectrum using natural light. Churnside and McGillivray⁷ made calibrated measurements on dead fish, and obtained a reflectivity in the backscatter direction that corresponds to a Lambertian reflectivity of 9 to 13%, depending on species. Most recently, Churnside et al.⁴ measured the reflectivity of live sardines in a seawater tank, obtaining equivalent Lambertian values of 9.7% for the polarization copolarized with the laser and 3.1% for the cross-polarized component.

We have made several airborne tests of lidar for detection of fish schools. In this paper, we describe the results of these tests. The next section is a description of the lidar system itself. Section 3 presents an example of the effects of receiver polarization on system performance. Section 4 presents an example of the differences between operation during the day and during the night. Section 5 is a description of the various signal processing techniques that have been used to date. Section 6 describes the flight tests that have been done. Section 7 presents examples of the results that have been obtained. The final section presents our conclusions and a discussion.

2 Lidar System

The lidar system is a non-scanning, radiometric lidar. A block diagram is presented in Fig. 1. The major components are (1) the laser and beam-control optics, (2) the receiver optics and detector, and (3) the data collection and display computer. The system also includes the capability to record aircraft position and attitude.

The laser is a frequency-doubled, *Q*-switched Nd:YAG laser that produces about 100 mJ of green (532 nm) light in a 12-ns pulse at a rate of 30 pulses/s. The laser is linearly polarized. The beam from the laser is diverged, with a lens in front of the laser, to produce a wide swath at night and a narrower swath during the day. The minimum divergence is

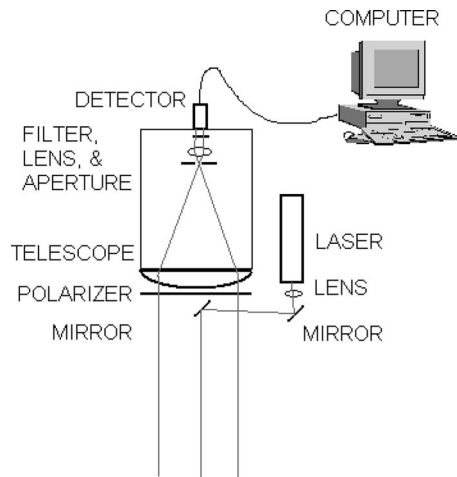


Fig. 1 Block diagram of lidar configuration.

determined by the requirement that the system be eye-safe at the surface [laser spot diameter of 5 m (Ref. 8)], so that the actual divergence angle depends on the altitude at which the aircraft is to be flown. This irradiance level is also safe for marine mammals.⁹ The maximum divergence is determined by the maximum field of view of the receiver (about 65 mrad).

The diverged beam is directed by a pair of mirrors to be parallel to the axis of the telescope. The figure shows a coaxial configuration of the transmitter and receiver. Sometimes this configuration is used, and sometimes a side-by-side configuration is used. While the coaxial configuration makes alignment easier at the short ranges available inside an aircraft hanger, there is no difference in the performance of the two configurations in flight.

The receiver optics use a 17-cm-diam refracting telescope. A polarizer is placed on the front of the telescope to select either the component of the return that is co-polarized with the laser or the cross-polarized component. Generally, the cross-polarized component is used, because our experience suggests that this component produces the best contrast between fish and the scattering from small particles in the water. The telescope collects the light onto an interference filter to reject background light. An aperture at the focus of the primary lens also limits background light by limiting the field of view of the telescope to match the divergence of the transmitted laser beam. During the day, a narrow field of view and a narrow interference filter are used to reject solar background light. At night, a larger field of view is used. This enables us to collect more multiply scattered photons and reduces the attenuation by the water. A reduction in the attenuation coefficient will produce greater depth penetration for the same dynamic range of the system.

High-speed digitizers exist that plug directly into the bus of personal computers, but these are limited to 8 bits of resolution. This produces 255 possible levels, which is not as much dynamic range as we would like for fish lidar applications. We considered two techniques to improve the dynamic range. In the first, the detector output is fed into a logarithmic amplifier. The output of the logarithmic amplifier is fed into the digitizer. The particular amplifier we used has a response of

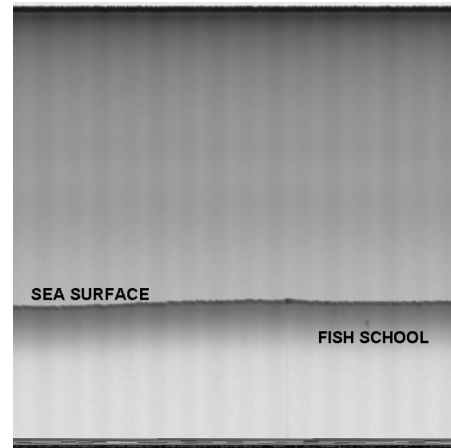


Fig. 2 Raw data file from receiver with logarithmic amplifier. Vertical dimension represents distance from the lidar; horizontal dimension represents distance along the flight track. The darker band just below the center of the image is the sea surface. The band at the bottom is an image interpretation of time, position, etc.

$$V_{\log} = -0.125 \log_{10}(-V_{\text{linear}}) - 0.486. \quad (1)$$

It has an input voltage range of -0.2 mV to -2 V, which corresponds to an output voltage range of about -0.024 to -0.524 V. Since the output voltage range is well within the range of an 8-bit digitizer, the logarithmic amplifier increases the maximum possible dynamic range from 255 to about 10^4 .

The other technique uses two digitizer boards with a 30-dB difference in sensitivity. One captures the strong signal near the surface but does not have the sensitivity to respond to weak signals from greater depths. The other saturates near the surface but is sensitive enough to capture the signals from greater depths. The maximum dynamic range of this combination is about the same as with the logarithmic amplifier.

The unprocessed data can be displayed as a gray-scale image, where depth is the vertical axis, time along the flight track is the horizontal axis, and the magnitude of the lidar return is presented as the gray level, where black is a strong signal, and white is zero signal. Figure 2 is a plot of the raw data for a typical example using the logarithmic amplifier. The intensity represents the logarithm of the signal. The dark band near the center of the image is the strong scattering region near the surface. The band at the bottom of the image is just an image representation of other information [global positioning system (GPS) information, aircraft attitude, etc.] and should be ignored. Fish can be seen as darker spots in the image.

Figure 3 is a similar plot for the dual digitizer system. The top half of the image represents the data from the low-gain channel, and the bottom half represents the data from the high-gain channel. In each case, the dark band represents the surface. Dark spots are schools of fish. The strongest school can be seen on both channels. As before, the dark band at the bottom of the image is the representation of the other information.

The information recorded at the end of each pulse includes aircraft position from the aircraft GPS, GPS time, the voltage applied to the photomultiplier tube (PMT), and

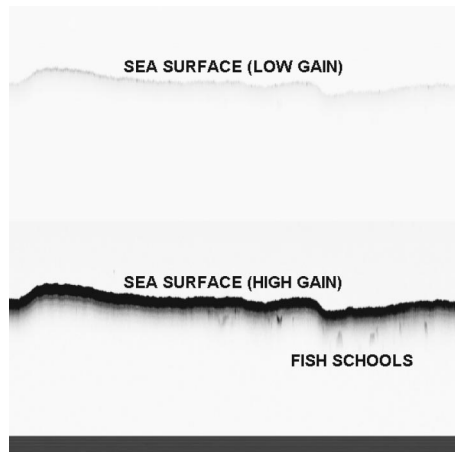


Fig. 3 Raw data from receiver with two linear amplifiers. Top half is signal from the low-gain channel; bottom half is signal from the high-gain channel.

the attitude of the aircraft as measured by tilt meters and laser gyroscopes on the optical package. The applied voltage on the PMT is used to find the gain of the tube, which is necessary for calibration. The computer records the data in files of 30- or 60-s duration.

The computer is also used to display the data during the flight. Two displays are commonly used. One is a line plot of the lidar return signal as a function of depth. Either linear or logarithmic signal levels can be displayed. This display is updated at the lidar pulse rate. The other is a gray-scale image, where the vertical dimension represents depth, the horizontal dimension represents time along the flight track, and the intensity of the return is represented by the gray level. For either display, we can find the surface return and reference the rest of the return to it. This stabilizes jitter caused by timing errors in the electronics and by aircraft motion. We can also estimate the particulate or clear water return and subtract that, leaving a display that represents the scattering from fish only. The two-point estimate, described in Section 5, is used.

3 Polarization Effects

The effects of receiver polarization were investigated during the California flights by changing the polarization in flight. Figure 4 is an example of the signal voltage across the 50- Ω load as a function of depth. These curves represent 30-s averages of the signal just before and just after rotating the polarization. The voltage applied to the PMT was changed at the same time, so that the actual optical signal of the copolarized curve should be multiplied by 19.1 to get an equivalent optical power. Several features of these curves are typical. First, note that the peak optical return for the copolarized return is about an order of magnitude greater (after multiplying by 19.1) than the peak for the cross-polarized return. The attenuation for the two polarizations is similar. The average lidar attenuation coefficient between 5 and 10 m in depth for these two data periods was 0.19 m^{-1} for the copolarized return and 0.21 m^{-1} for the cross; the difference is probably not significant because the two data sets were separated by about 5 min of

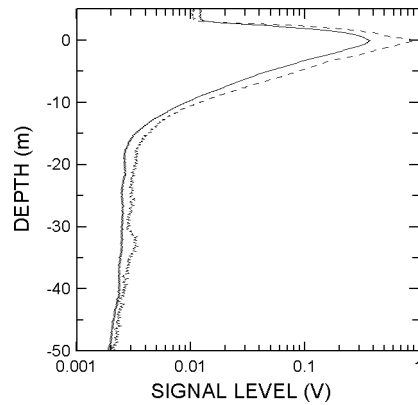


Fig. 4 Typical values for 30-s averages of single-pulse returns for copolarized light (solid line) and cross-polarized light (dashed line) without fish signals.

flight, or about 23 km. Despite the greater signal level for the copolarized return, the depth penetration for both polarizations is about 50 m.

Figure 5 shows single pulse returns within schools of fish in the same area. In both cases, there is a school between 5 and 10 m in depth. In the cross-polarized return, it is clearly visible as a bump on the exponentially decaying signal. A bump is also present on the copolarized return but is nearly imperceptible. To recognize this as a school of fish, it is necessary to look at a succession of returns, as is done on the aircraft. One can then see very small changes in signal. While these two returns are not from the same school of fish, they are typical of returns seen in the same region before and after changing polarization. Note also that the cross-polarized return is much noisier than the copolarized return. This is a direct consequence of the lower signal level in the cross polarization.

The observation here is that the contrast is better in the cross polarization than in the copolarization. This is consistent with laboratory results using a painted target.¹⁰

4 Day/Night Effects

The relative performance of day and night operations was investigated during the Bay of Biscay flights by flying the

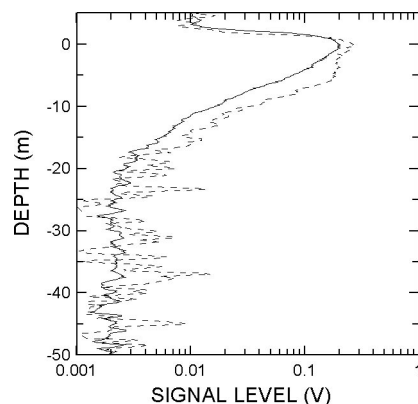


Fig. 5 Typical single-pulse returns (no averaging) for copolarized light (solid line) and cross-polarized light (dashed line) with fish signals.

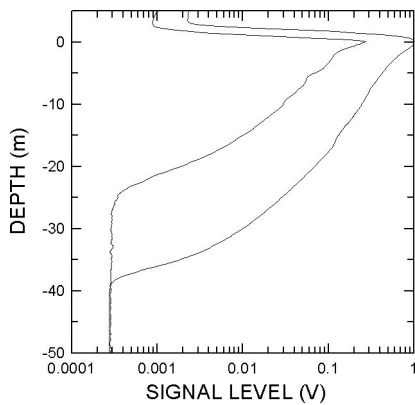


Fig. 6 Typical single-pulse returns for day (smaller signal) and night operations.

same pattern during the day and at night. Figure 6 is a plot of the average signal over 1-min periods taken at about 10:30 on 8 September and at about 19:30 on 9 September. Both were taken in the vicinity of 44 N 2.2 W. The main difference is in depth penetration. The penetration for the day case is about 25 m, while the nighttime case extends down to 40 m in this location. The primary reason is that the increased field of view used at night reduces the lidar attenuation coefficient.¹¹ The average lidar attenuation coefficient for these two data segments in the region between 5 and 10 m in depth was 0.086 m^{-1} during the day but only 0.052 m^{-1} at night. Overall, the median depth penetration for these two flights was 36 m at night but only 20 m during the day.

5 Signal Processing

The raw data are returned to the laboratory for processing. For the dual board receiver, the two signals must be combined into a single estimate of the return. Then, the surface position is located for each lidar pulse, the contribution to the signal from background light is estimated and removed, and the contribution to the signal from particulate scattering in clear water is estimated and removed. In this paper, we use clear water to refer to seawater plus its normal load of particles, including plankton, but not including fish. The attenuation is estimated so that signal levels can be corrected for attenuation.

The simplest algorithm to locate the surface position is to find the largest signal that occurs after some fixed time period after the laser pulse. The delay is necessary because the return signal from the atmosphere near the aircraft can easily be larger than any signal from the water. This simple algorithm works well unless (1) fog produces a near-surface return that is stronger than the surface return, (2) a shallow bottom produces a stronger return, or (3) fish near the surface produce a stronger return.

The contribution to the signal from the background light is easy to estimate. We simply use the average of the last 100 samples for each shot. The sampling times are set to ensure these samples occur well after the laser energy has decayed to zero.

The contribution from particulate scattering is more difficult. There is no way we can tell the difference between the signal scattered from fish and the signal scattered from

anything else using just one sample. We must assume that the clear water contribution has some uniformity so that its value within a school can be estimated. We tried two different techniques, each having advantages and disadvantages, depending on the water properties. The first assumes that the water is uniform in depth, although the properties may vary greatly from pulse to pulse. The second assumes that the water is uniform at any depth for some distance along the flight track, although the properties may vary greatly as a function of the depth.

The first signal processing technique we will call the two-point method because it uses a two-point fit to estimate the clear-water scattering. In uniform water, the lidar return will decay exponentially as a function of scattering depth in the water because of absorption and scattering. It will also experience a range-squared loss. We can express this mathematically by

$$S_w(z) = \frac{a \exp(-2\alpha z)}{(n\theta h + z)^2} + b, \quad (2)$$

where S_w is the linear signal; a is an amplitude parameter that includes such things as laser pulse energy, surface losses, receiver area, detector responsivity, etc., as well as the backscatter coefficient of the water; α is the lidar attenuation coefficient; z is depth; h is the height above the surface; n is the index of refraction of water; θ is the ratio of the cosine of the angle of the transmitted beam and the cosine of the incidence angle; and b is the background signal level. This equation is valid at depths below direct surface reflections.

Note that the range squared term in the denominator of Eq. (2) should contain the sum of the optical path length in air and the optical path length in water. In air, the path length is h divided by the cosine of the incidence angle. In water, it is z divided by the cosine of the angle of the transmitted beam and divided by n . This leads to Eq. (2) by letting the amplitude parameter a include the extra factors. For our nominal incidence angle of 15 deg, the transmitted beam is about 11 deg from the normal, and θ has a value of about 1.02; for our purposes, this can generally be neglected.

Two depths are selected, one just below any surface effects and one near the bottom of the useful lidar signal. The logarithms of these signals are used to infer a and α . Some averaging is generally done at the greater depth to reduce the effects of noise. A typical pulse return with no fish is shown in Fig. 7. Note that this pulse contains a significant surface signal. This is typical of the situation in rough water, where the wave slope can exceed the 15 deg tilt of the lidar and where foam and spray can produce a significant return. In low-wind conditions, the linear region often extends clear to the surface, and the surface is used as the top point for the fit. Figures 4 and 5 are more typical of low-wind conditions.

If fish are present at some depth, there is an additional contribution to the signal at that depth that depends on the backscatter coefficient of the fish, so

$$S(z) = a \left[1 + \frac{\beta_f(z)}{\beta_w} \right] \frac{\exp(-2\alpha z)}{(n\theta h + z)^2} + b, \quad (3)$$

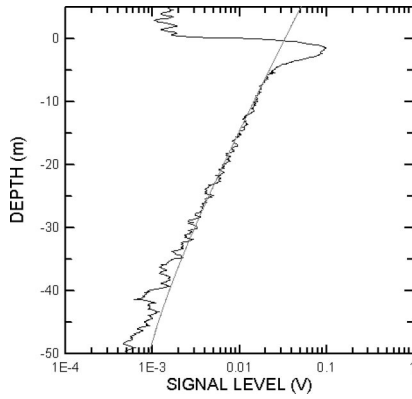


Fig. 7 Typical single-pulse return from clear water with two-point fit.

where β_f and β_w are the backscatter coefficients of the fish and water, respectively. The backscatter from fish is a function of depth for each pulse, but we have assumed that the attenuation of light by the fish can be neglected. As long as there are no fish at the two depths that we chose to get a and α , we can use the same procedure to get the particulate scatter, even when there are fish in the beam. If fish are at those depths, different depths are selected. Currently, this has to be done manually.

Thus, we can obtain the backscatter coefficient of fish, normalized by the backscatter coefficient of the water, from Eq. (3):

$$\frac{\beta_f(z)}{\beta_w} = \frac{S(z) - b}{a} (n\theta h + z)^2 \exp(2\alpha z) - 1. \quad (4)$$

This quantity, which we call the contrast, is used to obtain echo-sounder-like images.

In areas where the water properties vary with depth, the processing technique just described runs into problems. Variations of the scattering properties of the water with depth can be interpreted as fish. In this case, the results depend strongly on the choice of depths used in the fit. This is especially important in developing quantitative estimates of fish biomass. Because of these limitations, we have developed a different signal processing approach; this one is based on the assumption that the scattering properties of the water are uniform horizontally rather than vertically over some distance.

The specific signal processing technique is as follows. We break our files up into roughly 30-s segments. This corresponds reasonably well to the 1 nautical mile averaging lengths often used in acoustic surveys. The background water scattering signal at each depth is estimated by taking the median of the values from each shot at that depth. This provides an estimate of the depth profile of the water signal that is subtracted from each shot in the 30-s segment. The choice of the median value was made after some deliberation. If more than half of the pulses in some data segment are scattered from fish at a particular depth, the estimate of the water signal will be biased high because of the additional scattering from fish. We can eliminate this effect by using the minimum signal at each depth rather than the

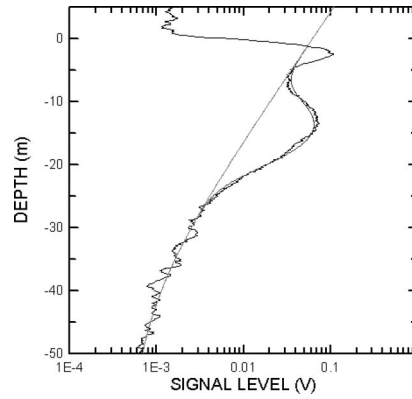


Fig. 8 Typical single-pulse return with fish signal with two-point fit to clear-water return and Gaussian fit to fish return.

median. However, this estimator would always be biased low because of noise effects. The median seems to do the best for the most cases.

Once our estimate of the water signal was subtracted from each shot, we normalize the remaining signal by the estimated water signal at each depth. This gives us the ratio of fish signal to water signal at each depth. To account for attenuation in propagation from the surface to each depth, we would like then to multiply this ratio by the water signal at the surface. However, the water signal at the surface can be strongly affected by surface scattering. Therefore, we instead multiply by the water signal at a depth of 5 m. We then measure the lidar attenuation coefficient of the water signal at 5 m and use this to project the value back to the surface. Thus, for each shot, we calculate the fish scattering signal as

$$S_f(z) = \frac{S(z) - S_w(z)}{S_w(z)} S_w(z = 5\text{ m}) \exp(10\alpha). \quad (5)$$

This signal is thresholded at a value where $S(z) = 2S_w(z)$ to reduce the contribution from noise. In addition, we required that a signal above threshold be present in at least two consecutive shots to be considered.

In the previous discussion, the multiplication by the water signal at the surface is only necessary if a quantitative measurement is desired. If the objective is to describe the relative distribution of fish, this is not needed; it is only a scale factor.

To automatically identify fish, we fit the contrast to a Gaussian function of depth for each pulse. The Gaussian was chosen because it is a convenient mathematical function to represent a layer. Even where there is structure within the layer that is not represented by the Gaussian, moments of the Gaussian can be used to estimate the integrated return, the mean depth, and the root mean square thickness of the layer.

A typical pulse with fish is shown in Fig. 8, along with the model fit from Eq. (2) that includes the Gaussian approximation for the contrast. The fit does not include a model for the surface return, and this portion (above a depth of about 5 m in this case) is neglected. Based on experience, the software flags a possible school of fish if the peak value of the Gaussian is greater than the water

return at the same depth for five consecutive lidar pulses. When the two-point fit is used, this technique can produce a high false alarm rate in regions with a definite plankton layer but did not seem to miss significant concentrations of fish. The false detections generated by this process can easily be eliminated manually.

To estimate integrated target strength, we start with the signal from which the clear-water return has been subtracted. Each lidar pulse is integrated over depth in a series of depth bins from the surface to the maximum depth. These bins typically are 5 m thick. The maximum depth is defined as the first sample that is less than the background light level; at this point, the signal is assumed to be down to the noise level. It occasionally happens that strong fish returns occur deeper than this, and the current algorithm misses these fish. However, there is always noise from depths below where we get a reliable clear-water signal; when we correct these noise values for assumed lidar attenuation, we get wildly varying results that distort the results. The effects of noise are reduced by ignoring any fish signals that are not greater than the clear-water return for at least three consecutive shots. The effects of occasional surface glint returns are reduced by ignoring any signal that is located at the surface. The single shot values are then averaged (not integrated) over some time or track length.

Calibration was performed using the following relationship to obtain an estimate of the integrated echo strength D in kg m^{-2} :

$$D = \frac{2n}{EAcT\eta\gamma^2} \frac{2\pi aLd}{r} \int_{z_1}^{z_2} \left(\frac{z}{n} + h\right)^2 S_f(z) dz, \quad (6)$$

where n is the index of refraction of water, h is the height of aircraft above the surface, E is the laser pulse energy, A is the receiver telescope area, c is the speed of light in vacuum, T is the transmission of the optics, η is the photocathode responsivity, γ is the surface transmission, a is the ratio of the cross-sectional area to the square of the length of the fish, L is the fish length, d is the density of water, r is the reflectivity of the fish, z_1 is the depth at the bottom of the integration depth bin, z_2 is the depth at the top of the bin, and S_f is the fish signal as seen in the photocathode current. This signal is calculated from the recorded voltage, the load resistance, and the electron gain of the PMT, which is a measured function of the applied voltage. For reflectivity, we use the results of Ref. 4.

6 Flight Tests

With minor variations in hardware and software, we have flown this basic system in four sets of flights.

The first was a set of flights over the Southern California Bight. The aircraft is a Beech KingAire, owned and operated by the California State Department of Fish and Game. This aircraft has two removable floor panels. Bins have been constructed to fit over these openings, and these bins are used to stock mountain lakes from the air. We constructed a flat plate that bolts over one of these openings, and the lidar optics package was mounted onto this. It was tilted back at an angle of 15 deg to reduce the specular reflection from the sea surface. The laser power supply, computer, and timing electronics were mounted in a stan-

dard equipment rack that was attached to the seat rail just in front of the optics package. The operator sits in front of the rack, facing rearward.

Twelve flights were made between March 30 and April 21, 1997. Seven of these flights were made during the day and five at night. Flight altitude was typically 100 m for the day flights and 300 m for the night flights.

The next set of flights was two short flights over Puget Sound. These were made in a Cessna Cardinal, a four-seat, single engine plane. A down-looking window was installed in the rear of the aircraft, behind the pilot. The electronics were tied down behind the right front seat, which was turned to face rearward so the operator could operate the equipment. For this installation, a second mounting plate was built that bolted over the window and held the power inverter as well as the lidar. This installation also required that the standard alternator on the Cessna be replaced by a high-capacity model. A small GPS system was used to obtain position information.

Two flights were made on 5 May 1997, one in the afternoon and one at night. Flight altitude for both flights was 300 m. Both flights covered the same area. The area was determined by the maximum area that could be covered by boat during the night. Each transect was covered twice during the 40-min duration of each flight. This aircraft is a very inexpensive way to cover limited areas. The pilot is a scientist within our laboratory, and the aircraft cost for these surveys was about \$0.50/mile. However, this aircraft is probably too small for large, precise surveys. The pilot must fly and navigate without an autopilot, which is difficult to do for extended periods. Also, a single-engine aircraft is probably not suitable for operation off shore, especially at night.

The third test was a series of 13 flights over the Atlantic near the coast of the Iberian Peninsula. These were made in a Casa aircraft owned and operated by the Spanish Space Agency, INTA. This is a twin-engine turboprop cargo plane. It has two large, down-looking openings in the cargo area. The lidar was mounted over the forward of these using another mounting plate. A Daedalus multispectral imager was mounted over the rear window. The lidar electronics were mounted in a rack forward of the openings.

Both day and night flights were conducted at an altitude of 300 m. One unexpected operational difficulty was encountered during the night flights; there are no airports along the Atlantic coast of Spain that are open 24 h a day.

The final two flights were made in the southern California Bight. Only night flights were made, as the object was to fly over areas where squid were being fished using floodlights. These were made in the same California State Fish and Game aircraft that was used before. Because of this, the installation was very quick. We were able to start the installation in Sacramento on Monday morning, finish in the early afternoon, and then fly to our base of operations in Long Beach. Our first data flight was that same evening, and the second was on Tuesday evening. On Wednesday morning, we returned to Sacramento, removed and packed the lidar, and went home to Colorado. This ease of installation and downloading allows us to be very flexible in scheduling surveys.

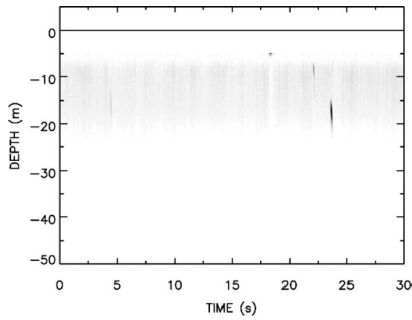


Fig. 9 Processed gray-scale image of a single large animal (probably a whale from the signal strength) in the Southern California Bight.

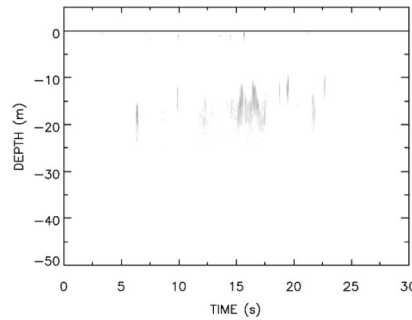


Fig. 11 Processed gray-scale image of a group of schools of sardines in an inlet in northwestern Spain.

7 Results

The primary result of the lidar system is a gray-scale image with the clear-water return removed. This type of image was patterned after typical echo sounder displays so that it would be familiar to fisheries’ biologists. In these images, we see several different types of fish signatures. Here, we present a few examples.

Figure 9 is an image of a very large single animal, probably a whale based on the strength of the return signal. While the nominal depth resolution of the lidar is just over 1 m, very strong targets like this can be seen by the tails of the laser pulse and appear to extend over greater depths. This image was obtained some distance from the shore off southern California.

Figure 10 shows a school of anchovies within a plankton layer. This image was obtained near the southern Californian coast. In this case, the plankton layer was a weak scattering layer extending for many kilometers. Fish could be identified within this layer as smaller regions of stronger scattering. This image was processed using the two-point method. This method retains the signature from the enhanced scattering layer; the median method would remove the signature from the plankton, leaving only the fish. Figure 11 is an example of several small schools of juvenile sardines in one of the inlets of northwestern Spain. It was processed using the median method. They are also within a plankton layer, but the median signal from this layer has been removed. The fish show up much more clearly with this processing technique, but the information about the

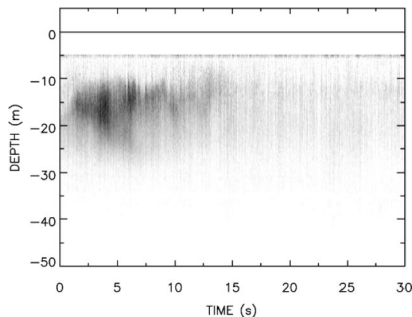


Fig. 10 Processed gray-scale image of a school of anchovies in the Southern California Bight.

plankton layer has been lost. In these cases, the depth profiles do not have the characteristic shape of the tail of the pulse, and represent real vertical structure in the scattering density.

The next product is a map of the locations of fish detections. This enables us to get a general feeling of where along the flight track fish were detected. Figure 12 is an example from the Southern California Bight. The solid line is the flight track for the night flight on 6 April, 1997. The symbols mark the locations of 30-s segments of the flight that contained fish as identified by the Gaussian detection algorithm. To create this map, several false detections were eliminated in areas where the algorithm mistakenly identified bottom return as fish. The three detections away from the shore were individual large animals, with returns similar to those of Fig. 9. The rest were anchovies within a large plankton layer. Identification of the fish as anchovies was by egg samples from a surface ship.

Finally, we can look at the depth distribution of fish using integrated echo strength. This is a typical product from echo sounders used by fisheries’ managers. Even where these data are not calibrated, they are very useful as indices of abundance that enable comparisons of relative concentrations of fish at different locations and different

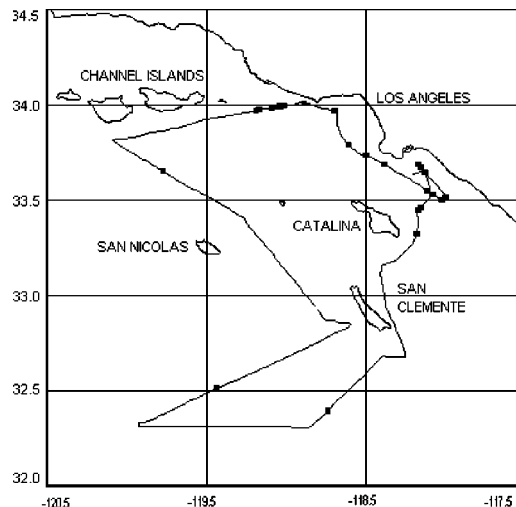


Fig. 12 Map showing locations of fish detections in the Southern California Bight.

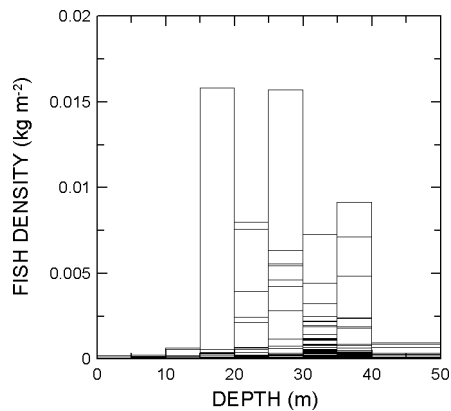


Fig. 13 Plot of measured biomass depth distributions (30-s averages).

times. Figure 13 presents a typical example from the Bay of Biscay. Each bar represents the average over 30 s of data, which corresponds to just over 2 km of flight track. We see that most of the biomass was located between 20 and 40 m.

8 Conclusions and Discussion

The primary conclusion we reached is that plankton layers, fish schools, and large single animals can be observed by an airborne lidar. These three types of targets can be discriminated one from another very reliably by a human operator. Automated fish detection algorithms have been developed that work well when the water scattering properties in the absence of fish are uniform either vertically down to the maximum penetration depth of the lidar or horizontally over 2-km segments of the flight track. The three main data products obtained from fisheries' echo sounders can also be obtained from an airborne lidar; these are depth-range gray-scale images, maps of fish locations, and integrated target strengths.

The greatest improvements to performance of this type of lidar are likely to come through improved data processing algorithms. This conclusion is based on the fact that a human can extract information from the data that the current software cannot. One example is the discrimination between fish and the bottom. Automatic identification of the bottom would enable much more accurate measurements in shallow water. Another area is in estimation of the clear-water signal. We currently assume uniformity in either the vertical or horizontal dimension. A much better approach would be to use the data to infer the scales of variations of the scattering properties of the water in both dimensions and estimate the clear-water return using the appropriate scales in both dimensions.

While the airborne lidar can produce data similar to an echo sounder at much greater survey rates, it also shares a couple of the problems of the echo sounder. The first of these is species identification. There is no feature of the lidar return that is unique to a particular species, and other information must be used. Generally, one can reduce the possibilities to just a few by habitat (location, time of year, position in the water column, etc.). Visual observations can also be used. In the Southern California Bight, the most

common schooling fishes are sardines and anchovies. Spotter pilots can reliably distinguish between these by direct observation during the day and by the mechanically induced bioluminescence at night, provided the schools are shallow enough to be seen. Automation of this capability using low-light video and sophisticated image processing is a possibility for the future.

Acknowledgments

We would like to express our appreciation to the pilots of the California State Department of Fish and Game, the pilots and crew of the 403rd Squadron of the Spanish Center of Cartography and Photography, and Dr. Jay Palmer of the National Oceanic and Atmospheric Administration/Environmental Technology Laboratory (NOAA/ETL). Dr. John Hunter and other scientists at the NOAA SouthWest Fisheries Science Center have provided invaluable guidance and support. This work was partially supported by the European Commission Programme on Agriculture and Fisheries project FAIR PL97-3374.

References

1. J. L. Squire Jr. and H. Krumboltz, "Profiling pelagic fish schools using airborne optical lasers and other remote sensing techniques," *Mar. Technol. Soc. J.* **15**, 27-31 (1981).
2. D. L. Murphree, C. D. Taylor, and R. W. McClendon, "Mathematical modeling for the detection of fish by an airborne laser," *AIAA J.* **12**, 1686-1692 (1974).
3. M. K. Krekova, G. M. Krekov, I. V. Samokhvalov, and V. S. Shamaev, "Numerical evaluation of the possibilities of remote sensing of fish schools," *Appl. Opt.* **33**, 5715-5720 (1994).
4. J. H. Churnside, J. J. Wilson, and V. V. Tatarskii, "Lidar profiles of fish schools," *Appl. Opt.* **36**, 6011-6020 (1997).
5. K. Fredriksson, B. Galle, K. Nyström, S. Svanberg, and B. Öström, "Underwater laser-radar experiments for bathymetry and fish-school detection," GIPR-162 Göteborg Institute of Physics, Göteborg, Sweden (1978).
6. J. A. Benigno and D. J. Kemmerer, "Aerial photographic sensing of pelagic fish schools: A comparison of two films," in *Proc. American Society of Photogrammetry Symp. on Remote Sensing in the Ocean*, Lake Buena Vista, FL (1973).
7. J. H. Churnside and P. A. McGillivray, "Optical properties of several Pacific fishes," *Appl. Opt.* **30**, 2925-2927 (1991).
8. *Safe Use of Lasers, Standard Z-136.1*, American National Standards Institute, New York (1993).
9. H. M. Zorn, J. H. Churnside, and C. W. Oliver, "Laser safety thresholds for cetaceans and pinnipeds," *Marine Mammal Sci.* **16**, 186-200 (2000).
10. G. D. Lewis, D. L. Jordan, and P. J. Roberts, "Backscattering target detection in a turbid medium by polarization discrimination," *Appl. Opt.* **38**, 3937-3944 (1999).
11. H. R. Gordon, "Interpretation of airborne oceanic lidar: effects of multiple scattering," *Appl. Opt.* **21**, 2996-3001 (1982).



James H. Churnside received his PhD in physics from the Oregon Graduate Center, Beaverton, in 1978. He was a member of the technical staff of the Aerospace Corporation in El Segundo, California, until 1985, when he moved to the Environmental Technology Laboratory of the National Oceanic and Atmospheric Administration (NOAA), where he is currently chief of the Ocean Remote Sensing Division.



James J. Wilson received his BS degree in electrical engineering technology from Metropolitan State College, Denver, Colorado, in 1986. He is currently an electronics engineer with the National Oceanic and Atmospheric Administration Environmental Technology Laboratory. His interests include high frequency electronics, optics and lidar. He has been working with fish lidar for the last 6 years.

Viatcheslav V. Tatarskii: Biography not available.